Inorganics **2014**, *2*, 132-154; doi:10.3390/inorganics2020132

OPEN ACCESS

inorganics

ISSN 2304-6740

www.mdpi.com/journal/inorganics

Article

Comparative Issues of Cathode Materials for Li-Ion Batteries

Christian M. Julien [1,*], Alain Mauger [2], Karim Zaghib [3] and Henri Groult [1]

[1] Physicochimie des Electrolytes et Nanosystèmes Interfaciaux (PHENIX), Université Pierre et Marie Curie—Paris6, UMR 8234, 4 place Jussieu, Paris 75005, France;
E-Mail: henri.groult@upmc.fr

[2] Institut de Minéralogie, de Physique des Matériaux et de Cosmochimie (IMPMC), UPMC Université Paris 06, 4 place Jussieu, Paris 75005, France;
E-Mail: alain.mauger@impmc.jussieu.fr

[3] Energy Storage and Conversion, Research Institute of Hydro-Québec, Varennes, QC J3X 1S1, Canada; E-Mail: zaghib.karim@ireq.ca

* Author to whom correspondence should be addressed; E-Mail: christian.julien@upmc.fr; Tel.: +33-144-273-534; Fax: +33-144-278-234.

Received: 29 January 2014; in revised form: 10 March 2014 / Accepted: 12 March 2014 / Published: 25 March 2014

Abstract: After an introduction to lithium insertion compounds and the principles of Li-ion cells, we present a comparative study of the physical and electrochemical properties of positive electrodes used in lithium-ion batteries (LIBs). Electrode materials include three different classes of lattices according to the dimensionality of the Li^+ ion motion in them: olivine, layered transition-metal oxides and spinel frameworks. Their advantages and disadvantages are compared with emphasis on synthesis difficulties, electrochemical stability, faradaic performance and security issues.

Keywords: lithium-insertion compounds; Li-ion batteries; phase diagram; safety

---

1. Introduction

Since three decades, lithium-ion batteries (LIBs) have been amongst the most promising chemical-electrical energy converter (rechargeable or secondary sources) for power electronic devices such as cellular phones, laptop computers, camera, *etc.* In 1992, the commercial success of LIBs based on carbon, a non-aqueous electrolyte, and lithium cobaltate ($LiCoO_2$) offered great promise as being

the first rechargeable battery technology for personal electronics in the near future [1]. Today, this technology is applied to green transportation systems such as electric vehicles (EVs) or hybrid EVs (HEVs). The increase in the demand of highly functionalized applications always includes higher power density, higher energy density, excellent charge-discharge cycling performance, and more safety.

A key element that limits the performance of the batteries is the active element of the positive electrode, and it is also the most expensive part. From 1980 to present, continuous efforts have been devoted by Goodenough to propose and study oxides compounds based on transition-metal (TM) element with focus to those compounds that crystallize in structures that favour large mobility of the Li^+ ions in order to transfer energy during the redox reaction. Milestones were made in 1980 for the $LiCoO_2$ layered structure [2], 1986 for $LiMn_2O_4$ spinels [3,4] and 1997 for the Li*M*PO_4 (*M* = Fe, Mn, *etc.*) olivine family [5]. Rapidly, all these substances have been widely studied and effectively applied to the construction of commercial Li-ion batteries. Layered materials are used as cathodes for high-energy systems [6,7], while spinel oxides and olivines are considered in the case of high-power Li-ion batteries because low cost and long-life requirements, respectively [8,9]. However, these lithium-insertion compounds must fulfil specific properties such as chemical stability, capacity, rate capability, toxicity, cost and safety. All of them, however, achieve theoretical specific capacity >140 mAh g^{-1} at a potential >3.4 V *vs.* Li^0/Li^+. Table 1 summarizes the electrochemical properties of the three classes of insertion compounds.

Table 1. Electrochemical characteristics of the three classes of insertion compounds.

Framework	Compound	Specific capacity [a] (mAh g^{-1})	Average potential (V *vs.* Li^0/Li^+)
Layered	$LiCoO_2$	272 (140)	4.2
	$LiNi_{1/3}Mn_{1/3}Co_{1/3}O_2$	272 (200)	4.0
Spinel	$LiMn_2O_4$	148 (120)	4.1
	$LiMn_{3/2}Ni_{1/2}O_4$	148 (120)	4.7
Olivine	$LiFePO_4$	170 (160)	3.45
	$LiFe_{1/2}Mn_{1/2}PO_4$	170 (160)	3.4/4.1

[a] Value in parenthesis indicates the practical specific capacity of electrode.

This paper deals with the advantages and disadvantages of the positive electrodes materials used in Li-ion batteries: layered $LiCoO_2$ (LCO), $LiNi_yMn_yCo_{1-2y}O_2$ (NMC), spinel $LiMn_2O_4$ (LMO), $LiMn_{1.5}Ni_{0.5}O_4$ (LMN) and olivine $LiFePO_4$ (LFP) materials. Despite thousands of published papers considering the development of such materials, comparative studies of their properties as active electrochemical elements are rather scarce. It is our purpose to report difficulties of synthesis, electrochemical stability and performance, and security issues of these three classes of lattices from the point of view of Li^+ ion motion in them. As effective lithium-insertion compounds, special attention is given to the olivine $Li(Fe,Mn)PO_4$ that is considered as the most promising candidate for the next-generation of large-scale Li-ion batteries, not only for use in EVs or HEVs, but also to solve intermittence on smart grids and energy storage for high-power applications.

2. The Cell Potential (Goodenough Diagram)

The major contribution to the changes of the chemical potential during the intercalation process directly gives the open-circuit voltage of the battery such as

$$-eV_{oc} = \mu_{Li}(C) - \mu_{Li}(A) = \Delta\mu_e + \Delta\mu_{Li^+} \quad (1)$$

in which the chemical potential of the exchanged Li-atoms in anode (A) and cathode (C) is conceptually divided to the involved occupation of sites by Li^+-ions and the valence electronic density of states (DOS) by electrons. The charge compensation of exchanged Li^+-ions is compensated by redox reaction within the electrode, which leads to a modified occupation of electronic states.

For a given redox couple, the potential of an intercalation electrode considered as solution of guest A in the host lattice <H> is provided by the classical thermodynamic law

$$V(x) = -\frac{1}{zF}\frac{\partial(\Delta G)}{\partial x} + \text{constant} \quad (2)$$

where ΔG denotes the variation in the Gibbs energy of the system, x is the composition, z the number of electrons involved and F the Faraday's constant. $V(x)$ is thus the electrode potential as a function of the composition x in $<A_xH>$ [10].

Figure 1. Schematic diagram showing the electronic density of states and Fermi energies for an oxide-based electrode ($Li_xNi_{0.5-y}Mn_{1.5-y}Cr_{2y}O_4$ spinel material). The Li permeable solid electrolyte interface (SEI) layer formed on the electrode surface preserves the overall reversible reaction.

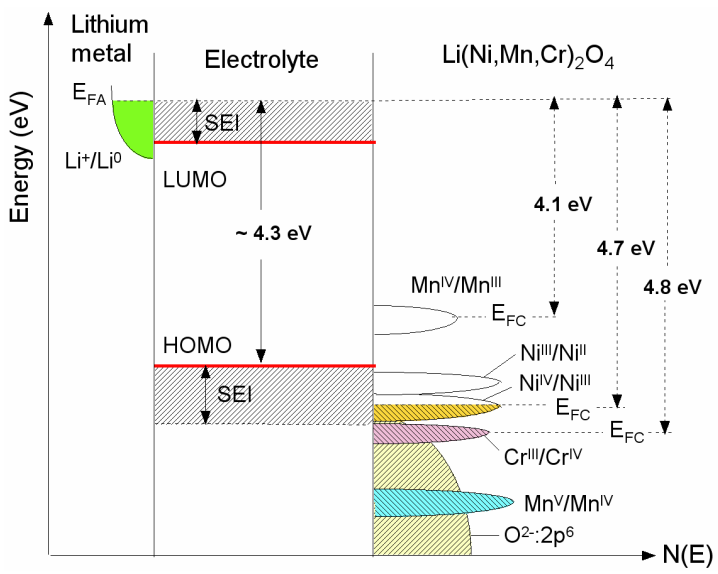

The open-circuit energy diagram of a lithium battery (see Figure 1) has been discussed by Goodenough *et al.* [11,12]. If the active transition-metal cation contains a localized *d*-electron manifold, the manifold acts as a redox couple, e.g., $Ni^{2+/4+}$ in $LiNi_{1.5}Mn_{0.5}O_4$ (LNM). Successive redox couples are separated by an on-site effective Coulomb correlation energy U that can be large when augmented by either a crystal-field splitting or an intra-atomic exchange splitting [13]. However, when the Fermi energy E_{FC} of the cathode material approaches the top of the anion p bands of the host,

the *p-d* covalent mixing may transform the correlated *d* electrons at E_{FC} into band electrons occupying one-electron states [11,14]. In the absence of a crystal-field splitting of the *d* orbitals at E_{FC}, which is the case for Ni(IV) to Ni(II), the one-electron states are not separated by any on-site energy *U* and there is no step in the voltage of the battery. E_{FC} is moved from one formal valence state to another upon the reduction or oxidation of the host.

3. Crystal Structure and Electronic Properties

The crystal structures of the three classes of Li-insertion compounds are shown in Figure 2. Their classification corresponds to the ion diffusion pathways and activation energy that govern Li-ion transport within the electrode materials [10]. Archetypes are the two-dimensional $Li[M]O_2$ with M = Co, Ni, (Ni_xCo_{1-x}) or ($Ni_xMn_yCo_z$), the three-dimensional $Li[X]_2O_4$ with X = Mn, ($Mn_{1-y/2}Li_{y/2}$) or ($Mn_{3/4}Ni_{1/4}$) and uni-dimensional $Li[M']PO_4$ with M' = Fe, Mn, Ni, Co or (Fe_yMn_{1-y}).

Figure 2. Crystal structure of the three lithium-insertion compounds in which the Li^+ ions are mobile through the 2-D (layered), 3-D (spinel) and 1-D (olivine) frameworks.

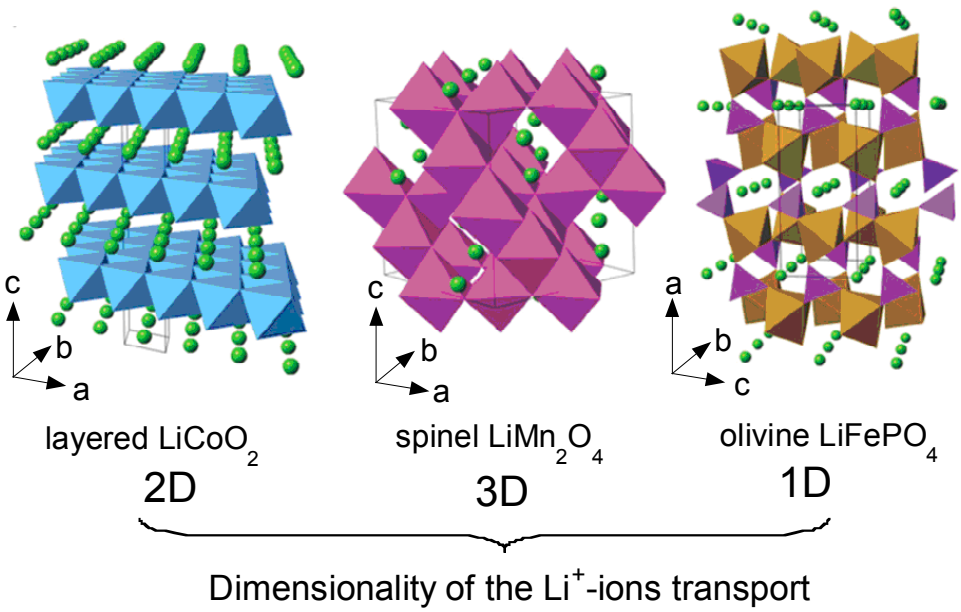

3.1. Layered Compounds

$Li[M]O_2$ (M = Co, Ni) oxides are isostructural to the layered α-$NaFeO_2$ (space group $R\bar{3}m$, No. 166) with the oxygen ions close-packed in a cubic arrangement and the TM and Li ions occupying the octahedral sites of alternating layers with an ABCABC… stacking sequence called "O3-type" structure (Figure 2). In $LiCoO_2$, the cobalt is trivalent in the electronic configuration $(t_{2g})^6(e_g)^0$, *i.e.*, in the low-spin state (S = 0). However, LCO adopts the rhombohedral symmetry in the high temperature form, with Li in 3*a*, Ni in 3*b* and O in 6*c* sites. The unit-cell of the hexagonal setting contains three formula units. During the cycling of a lithium cell, the Li^+ ions are reversibly removed from and incorporated into this framework creating or annihilating vacancies within the lithium planes as shown in Figure 2. These vacancies can indirectly drive electronic transitions in LCO or can organize the formation of ordered Li-vacancy structures on a triangular lattice of sites. Note that the low-temperature

form (LT-LCO) adopts the spinel lattice with the cubic symmetry (S.G. *Fd*3*m*) [15,16]. A lithium ordering and stacking sequences leading to an equivalent environment for all Co ions is preferred in order to achieve a maximum of charge delocalisation and to minimize the energy. In Li_xCoO_2, no coupling between Co:e_g and Li:2*s* states occurs and the lowest-energy is reached in the interplanar stacking that leads to as many equivalent Co sites as possible. This is consistent with a $Co^{+3/+4}$ tendency for charge delocalization at $x = 0.5$. In $Li_{0.5}CoO_2$, Co tends to have an intermediate oxidation state of +3.5 that induces a transition to a monoclinic structure [17]. Even worse, $LiCoO_2$ suffers from the dissolution of the metal ion in the electrolyte that induces oxygen release, which becomes more important upon increasing the temperature. Thus, surface modification by metal-oxide coating such as ZrO_2, Al_2O_3, TiO_2, *etc.* was demonstrated being an effective strategy to avoid the cathode breakdown [18,19].

$LiNiO_2$ (LNO) is isostructural with $LiCoO_2$ and has the *O3*-type-oxygen packing shown in Figure 2. The $Ni^{3+/4+}$ couple with high lithium chemical potential provides a high cell voltage of *ca.* 4 V like LCO. However, LNO suffers from a few drawbacks: (i) difficulty to synthesize $LiNiO_2$ with all the nickel ions in the Ni^{3+} valence state and distributed in a perfectly ordered phase without a mixing of Li^+ and Ni^{3+} ions in the lithium plane; $Li_{1-z}Ni_{1+z}O_2$ illustrates better the chemistry of this compound. (ii) Jahn-Teller distortion (tetragonal structural distortion) associated with the low spin Ni^{3+}:d^7 ($t_{2g}^6 e_g^1$) ion. (iii) Irreversible phase transitions occurring during the charge-discharge process. (iv) Exothermic release of oxygen at elevated temperatures and safety concerns in the charged state [20]. As a result, $LiNiO_2$ is not a promising material for commercial lithium-ion cells. However, mixed $LiNi_{1-y}Co_yO_2$ phases allow overcoming the main drawbacks exhibited by both $LiCoO_2$ and $LiNiO_2$ oxides [21–23]. For example, the solid solutions $LiNi_{0.85}Co_{0.15}O_2$ and $LiNi_{0.80}Co_{0.15}Al_{0.05}O_2$ have been shown to exhibit attractive electrochemical properties with reversible capacity of ~180 mAh g^{-1} and excellent cyclability [24].

3.2. $LiMn_2O_4$ (LMO)

$LiMn_2O_4$ belongs to the $A[B_2]O_4$ spinel-type structure and crystallizes in the *Fd*3*m* space group (O_h^7 factor group) with the cubic lattice parameter $a = 8.239$ Å [25]. The cubic spinel $LiMn_2O_4$ structure is described with the Mn and Li cations on the *16d* and *8a* sites, respectively, and the oxygen ions located on the 32*e* sites form a nearly ideal cubic close-packed (ccp) sublattice. Half of the octahedral interstices are occupied by the Mn ions forming a three-dimensional framework of edge-sharing MnO_6 octahedra. Lithium ions occupy tetrahedral sites, which share common faces with four neighboring empty octahedral sites at the *16c* position (Figure 2). This lattice offers a three-dimensional network of transport paths *16c-8a-16c* through which lithium ions diffuse during insertion/deinsertion reactions [3,4].

The understanding of the LMO spinel from the standpoint of solid-state chemistry must take into account the presence of oxygen vacancies revealed by neutron diffraction measurements, and is subject to debate. Two structure models were proposed for the "oxygen vacancy" phase: vacancy at the oxygen site corresponding to the formula $LiMn_2O_{4-\delta}$, and excess cations at the interstitial site with the formula $Li_{1+x}Mn_{2+y}O_4$ [26].

3.3. $LiNi_{0.5}Mn_{1.5}O_4$ (LNM)

Substitution of 25% Ni for Mn in $LiMn_2O_4$ spinel has been chosen because this composition implies that Mn is in the 4+ valence, thus avoiding the Jahn-Teller (JT) distortion associated to Mn^{3+}. Therefore, the electrochemical activity is only due to the oxidation/reduction of Ni^{2+} ions leading transfer of $2e^-$ per Ni ion. $LiNi_{0.5}Mn_{1.5}O_4$ crystallizes in two possible crystallographic structures according the cationic sublattice: the face-centred spinel (S.G. *Fd*3*m*) named as "disordered spinel" and the simple cubic phase (S.G. P_4332) named as "ordered spinel". The cation distribution in the P_4332 symmetry is then Li on 8*c*, Ni on 4*b*, Mn on 12*d*, and O(1) and O(2) oxygen ions occupy the 24*e* and 8*c* Wyckoff positions, respectively. The net result is thus a significant optimisation of space occupation leading to a reduced unit cell volume. It has been pointed out that phase-pure LNM is difficult to synthesize because impurities such as NiO and/or $Li_yNi_{1-y}O$ usually exist [27]. The partial replacement of Ni and Mn by Cr in $LiNi_{0.5-y}Mn_{1.5-y}Cr_{2y}O_4$ is an effective way to alleviate the problem of oxygen loss generating Mn^{3+} ions in the LNM framework and a voltage plateau at *ca.* 4 V *vs.* Li^0/Li^+. Thus, it has been demonstrated that the Cr-doping stabilizes the lattice without impacting the capacity significantly, but it decreases the energy density [28].

3.4. Olivine $LiFePO_4$ (LFP)

The crystal structure of $LiFePO_4$ materials has been studied by several authors [29–31]. As a member of the olivine family, LFP crystallizes in the orthorhombic system (*Pnma* space group, No. 62). It consists of a distorted hexagonal close-packed (hcp) oxygen framework containing Li and Fe located in half the octahedral sites and P ions in one-eighth of the tetrahedral sites. The FeO_6 octahedra, however, are distorted, lowering the regular octahedral O_h to the C_s symmetry. This structure illustrated in Figure 2 shows the channels via which the lithium ions can be removed. Corner-shared FeO_6 octahedra are linked together in the *bc*-plane, while LiO_6 octahedra form edge-sharing chains along the *b*-axis. The tetrahedral PO_4 groups bridge neighboring layers of FeO_6 octahedra by sharing a common edge with one FeO_6 octahedra and two edges with LiO_6 octahedra.

The $LiFePO_4$ structure consists in three non-equivalent O sites. Most of the atoms of the olivine structure occupy the 4*c* Wyckoff position except O(3) which lies in the general 8*d* position and Li^+ ions occupying only the 4*a* Wyckoff position (M_1 site on an inversion center). The Fe magnetic ions are in the divalent Fe^{2+} state and occupy only the 4*c* Wyckoff position (M_2 site in a mirror plane), *i.e.*, the center of the FeO_6 units. As a consequence, Fe is distributed so as to form FeO_6 octahedra isolated from each other in $TeOc_2$ layers perpendicular to the (001)-hexagonal direction [22]. In addition, the lattice has a strong two-dimensional character, since above a $TeOc_2$ layer comes another one vertical to the previous one, to build (100) layers of FeO_6 octahedra sharing corners, and mixed layers of LiO_6 octahedra and PO_4 octahedra. The lithium iron phosphate material differs from the primary mineral triphylite $Li(Mn,Fe)PO_4$ by the fact that triphylite is only rich in iron, with some manganese ions also in the M_2 site [32]. However, while the triphylite is a naturally occurring mineral, $LiFePO_4$ is an artificial product.

The energy diagrams *vs.* DOS showing the relative Fermi level of the Li-insertion compounds described in this Section are shown in Figure 3: the $Co^{4+/3+}$ redox couple for $LiCoO_2$, the $Ni^{4+/3+}$ redox

couple for $LiNi_{0.8}Co_{0.2}O_2$, the $Mn^{4+/3+}$ redox couple for $LiMn_2O_4$ and the $Ni^{3+/2+}$ redox couple for $LiNiPO_4$. Also, the cell voltage V_{oc} determined by the energies involved in both the electron transfer and the Li^+ transfer highlights the concept of rechargeable lithium batteries. While the energy involved in electron transfer is related to the work functions of the cathode and anode, the energy involved in Li^+ transfer is determined by the crystal structure and the coordination geometry of the site into/from which Li^+ ions are inserted/extracted. The stabilization of the higher oxidation state is essential to maximize the cell voltage and the energy density. The location of O:2*p* energy and a larger raising of the M^{n+}:*d* energies due to a larger Madelung energy make the higher valent states accessible in oxides. That is why transition-metal oxide hosts were pursued as positive electrode candidates for Li-ion secondary batteries [13].

Figure 3. Comparison of the energy *vs.* density of states showing the relative Fermi level of the $Co^{4+/3+}$ redox couple for $LiCoO_2$, the $Ni^{4+/3+}$ redox couple for $LiNi_{0.8}Co_{0.2}O_2$, the $Mn^{4+/3+}$ redox couple for $LiMn_2O_4$ and the $Ni^{3+/2+}$ redox couple for $LiNiPO_4$.

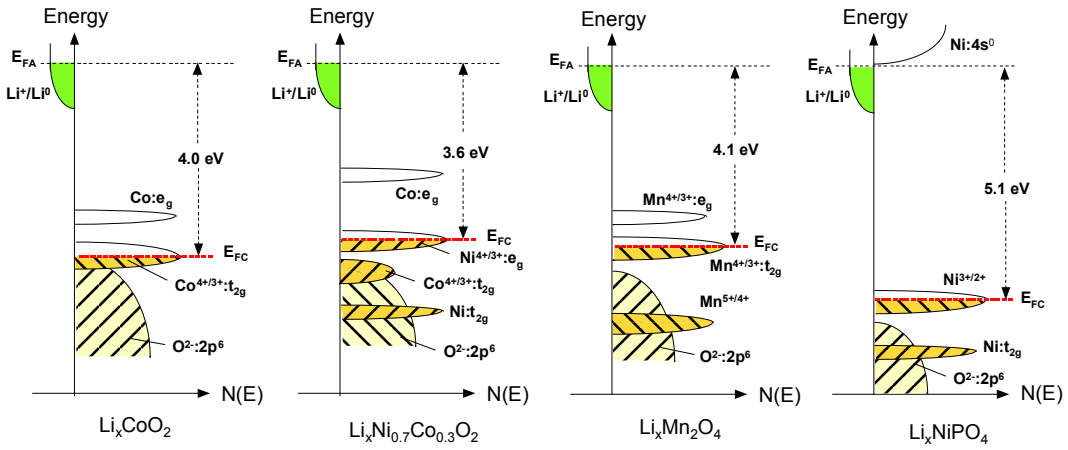

4. Electrochemical Properties and Phase Diagram

4.1. Lithium Cobaltate (LCO)

Li_xCoO_2 used as prototype positive electrode in LIBs. Charge-discharge curves Li_xCoO_2 at C/24 rate in the range 3.6–4.85 V *vs.* Li^0/Li^+ are shown in Figure 4. The sequence of the several phases is indicated as *x* varies from 1.0–0.05. $LiCoO_2$ has shown degradation and fatigue during electrochemical cycling. The change can be interpreted as an increasing energetic overlap of the Co:3*d* and O:2*p* states and a change in the orbital of Co and oxygen wave functions. For $1.0 \geq x \geq 0.5$, the DOS nearly does not change and the charge compensation with Li extraction leads to a removal of electrons from the Co:3*d* t_{2g} derived states with the Fermi level moving downwards (Figure 3).

Laubach *et al.* [33] have shown that the valence band (VB) is mainly unchanged with a slight shift of the top of the VB to lower binding energies, which implies a shift of E_{FC} that provokes the removal of *d*-electrons due to the change of the oxidation state from Co^{3+} to Co^{4+}. For $x < 0.5$, a clear increase in hybridisation occurs between the Co:3*d* and O:2*p* states associated with a reduction of the (CoO_6)-slab distances evidenced by the reduction of the c-axis lattice parameter. As a consequence, the

charge compensation of the delithiation leads to a removal of electrons from Co-O:*d-p* hybrid states, which translates to a partial oxidation of the O^{2-} ions [34–36].

Figure 4. Charge-discharge curves Li_xCoO_2 at C/24 rate in the range 3.6–4.85 V *vs.* Li^0/Li^+. The sequence of the several phases is indicated as *x* varies from 1.0–0.05.

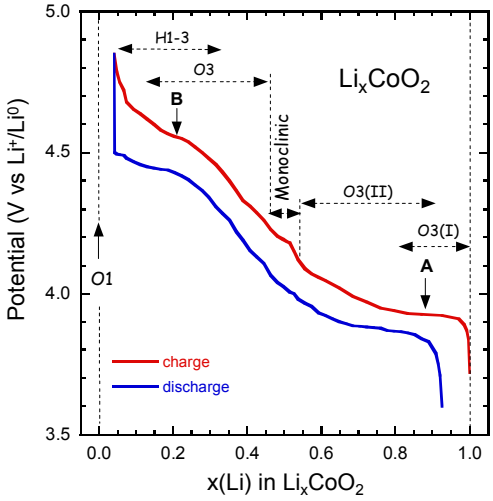

4.2. Lithium Manganese Spinel (LMO)

Manganese is five times cheaper than cobalt and is found in abundance in nature. The spinel $LiMn_2O_4$ has a strong edge-shared $[Mn_2]O_4$ octahedral lattice and exhibits good structural stability during the charge-discharge process. $LiMn_2O_4$ spinels have shown a lack of robustness in their cycle life and irreversible loss of capacity that becomes rapid at elevated temperatures [37].

The electrochemical data demonstrate that Li^+ ions are extracted from the tetrahedral sites of the $Li_xMn_2O_4$ spinel structure at approximately 4 V in a two-stage process, separated by only 150 mV [38] at a composition $Li_{0.5}Mn_2O_4$ (Figure 5). At $x = 0$, the λ-MnO_2 phase (λ-γ$[Mn_2]O_4$ in the spinel notation) is formed. The two-step process is due to ordering of the lithium ions on one-half of the tetrahedral 8*a* sites. In the spinel LMO, generally, Li at tetrahedral 8*a* site moves to vacant octahedral 16*c* site, and the 3-D 8*a*-16*c*-8*a*-16*c* network provides an energetically favourable pathway for the rapid diffusion of lithium in and out of the structure during discharge and charge, respectively.

Lithium insertion into LMO occurs at approximately 3 V. During this process, Li^+ ions are inserted into the octahedral 16*c* sites of the spinel structure. Since the 16*c* octahedra share faces with the 8*a* tetrahedra, electrostatic interactions between the Li^+ ions on these two sets of sites cause an immediate displacement of the tetrahedral-site Li^+ ions into neighboring vacant 16*c* octahedral sites. The reaction results in a first-order transition to $Li_2Mn_2O_4$ with a stoichiometric rock-salt composition on the surface of the electrode particle. The electrochemical process at 3 V is thus a two-phase reaction. During discharge, a reaction front of $Li_2Mn_2O_4$ moves progressively from the surface of the $LiMn_2O_4$ particle into the bulk. At 3 V, the Li insertion is accompanied by a severe Jahn-Teller distortion as a result of an increased concentration of Mn^{3+}:d^4 ions in the Mn_2O_4 spine1 lattice, which reduces the crystal symmetry from cubic (c/a = 1.0) to tetragonal symmetry (c/a = 1.16) that results in a 16% increase in the c/a ratio detrimental to the electrochemical cycling.

Figure 5. Voltage profile of a Li//$LiMn_2O_4$ cell discharged at C/24 rate with LMO material synthesized at 700 °C (**left**).Variation of the lattice parameters as a function of the Li content *x* during the charge/discharge in LMO cathode (**right**).

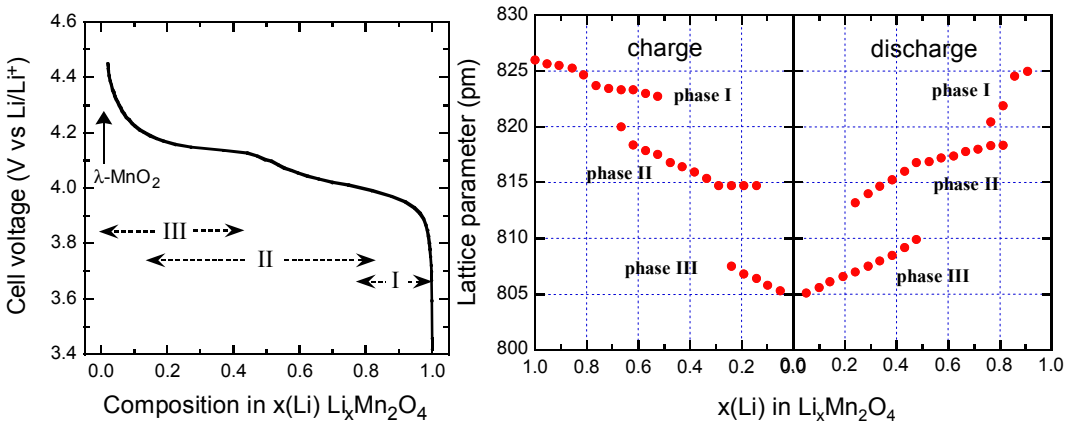

Xia *et al.* [39] showed by *in situ* X-ray diffraction that a two-phase structure coexists in the high-voltage region for LMO that persists during Li-ion insertion/extraction at low temperatures during cycling. Dai *et al.* [38] developed a mathematical model for the capacity fade of a LMO electrode by including the acid attack on the active material and the solid electrolyte interphase (SEI) film formation on the LMO particle surface. The acid generated by the $LiPF_6$ and the solvent decompositions are coupled to the Mn dissolution. The decrease of the Li ion diffusion coefficient is involved as another contribution to the capacity fade, which is caused by the passive film formation on the active material surface.

Several reasons have been proposed for the capacity loss of Li//$Li_xMn_2O_4$ cells in the 4-V region as follows [40,41].

(i) The major drawback is the disproportionation of Mn^{3+} at the particle surface in the presence of trace amounts of protons (acid attack) into Mn^{2+} and Mn^{4+}

$$2Mn^{3+}_{(solid)} \rightarrow Mn^{4+}_{(solid)} + Mn^{2+}_{(solution)} \quad (3)$$

resulting in a leaching out of Mn^{2+} ions from the positive electrode framework into the electrolyte [41]. Xia *et al.* [39] reported that chemical analytical results indicated that the capacity loss caused by the simple dissolution of Mn^{3+} accounted for only 23% and 34% of the overall capacity losses cycling at room temperature and 50 °C, respectively. The appropriate method to reduce capacity fade of LMO is surface coating of the particles to prevent the Mn^{2+} dissolution by a thin layer of inorganic material such as Al_2O_3 [42], zirconia [43], MgO [44], Li_2O-B_2O_3 glass [45], AlF_3 [46], *etc.* The use of surface treatment is an effective way to improve the elevated temperature storage properties of LMN spinels. This has been done by creating a protective barrier layer between the liquid electrolyte and the particle surface showing the importance of controlling the surface chemistry. Another way to avoid this problem has been to choose chemical composition such that Mn remains inactive in the 4+ valence state; this is the case for $LiNi_{1/3}Mn_{1/3}Co_{1/3}O_2$ and $LiNi_{1/2}Mn_{3/2}O_4$.

(ii) The instability of the delithiated spinel structure by oxygen loss in organic electrolyte solvents in the end of the charge.

(iii) The onset of a Jahn-Teller effect at the end of discharge (particularly at high current density). Under dynamic, non-equilibrium conditions above 3 V, it has been proposed that some crystallites can be more lithiated than others, thereby driving the composition of the electrode surface into a Mn^{3+}-rich $Li_{1+x}Mn_2O_4$ region [47,48].

Moreover, the specific capacity of spinel $LiMn_2O_4$ is limited to <120 mAh g^{-1} around 4.1 V *vs.* Li^0/Li^+, which corresponds to the extraction of 0.8 Li per formula unit. It has also pointed out that additional Li could be inserted into the empty octahedral holes of the spinel framework at a potential of ~3 V *vs.* Li^0/Li^+ accompanied by a structural change from cubic to tetragonal symmetry due to the Jahn-Teller distortion associated with the high-spin Mn^{3+} ($t_{2g}^3 e_g^1$) ions inducing a huge volume change and severe capacity fade. Evidence of structural fatigue has been detected by high-resolution electron diffraction and imaging, at the surface of discharged $Li_xMn_2O_4$ spinel electrodes in Li//$Li_xMn_2O_4$ cells [49]. Under non-equilibrium conditions, domains of tetragonal $Li_2Mn_2O_4$ coexist with cubic $LiMn_2O_4$, even at 500 mV above the voltage expected for the onset of the tetragonal phase. The presence of $Li_2Mn_2O_4$ on the particle surface may contribute to the capacity fade observed during cycling of Li//$Li_xMn_2O_4$ cells, due to the loss of particle-to-particle contact at the cubic-$LiMn_2O_4$/tetragonal-$Li_2Mn_2O_4$ interface in discharge state. *In situ* XRD has been used to study the $Li_xMn_2O_4$ ($0 \leq x \leq 1$) cathode materials during extraction and insertion of Li^+ ions.

Three-phase behavior is observed during the first charge-discharge cycle in the 4-V region (Figure 5). The voltage profile exhibits two plateaus at 4.05 and 4.15 V corresponding to two-phase systems induced by three cubic phases. $LiMn_2O_4$ is a small-polaron semiconductor, electronic conduction occurring via hopping of electrons between e_g orbitals on adjacent Mn^{3+}/Mn^{4+} cations. Thus, the gradual removal of Li^+ ions from the structure during deintercalation should result in a decrease in the number of mobile electrons throughout the whole solid [50].

4.3. Lithium Mn-Ni-Co Oxides

The layered $LiNi_yMn_yCo_{1-2y}O_2$ (NMC) compounds with a hexagonal single-phase α-$NaFeO_2$-type structure have received great attention as 4V-electrode materials to replace $LiCoO_2$ in Li-ion batteries, owing to its better stability during cycling even at elevated temperature, higher reversible capacity and milder thermal stability at charged state [51]. Its reversible capacity was measured to be 160 mAh g^{-1} in the cut-off range of 2.5–4.4 V and 200 mAh g^{-1} in that of 2.8–4.6 V [52]. The main problem that still needs to be solved for such applications of NMC is the cation mixing between nickel and lithium ions, since the ionic radius of Ni^{2+} (0.69 Å) is close to that of Li^+ (0.76 Å). The cation mixing between Li^+ and Ni^{2+} ions on the crystallographic (3*b*) sites of the NMC lattice is known to deteriorate their electrochemical performance. Rietveld refinement of the XRD data have demonstrated the validity of the structural model $[Li_{1-\delta}Ni_\delta]_{3b}[Li_\delta Ni_{x-\delta}Mn_yCo_{1-x-y}]_{3a}O_2$ (see detail in ref. [53]). Within a rigid-band model, the calculation of the relative position of the Fermi level and the O:2*p* band with respect to the $Ni^{4+/3+}$ and $Co^{4+/3+}$ redox couples for $LiNi_yMn_yCo_{1-2y}O_2$ as a function of x(Li) during the charge shows that in of 2.8–4.6 V potential region the NMC electrodes are more stable than LCO ones (Figure 6).

4.4. LMN and Doped-LMN Electrodes

The partial substitution of metal cations for the Mn forming the $LiMn_{2-y}M_yO_4$ and $LiMn_{1.5-y}Ni_{0.5-y}M_{2y}O_4$ solid solutions (with M = Ni, Cu, Cr) is a strategy to improve significantly the electrochemical cycling of $LiMn_2O_4$ materials, but at the expense of a decrease in the initial capacity within the useful voltage window, *i.e.*, below 4.4 V. Such a successful result is due to the reduction of the concentration of the Mn^{3+} JT ions that provokes the tetragonal phase transition in the 3-V region. As an example, the early work of Ein-Eli and Howard [54] showed by cyclic voltammetry measurements that Cu substitution for Mn in LMO exhibited two discharge regimes, at 4.1 and 4.9 V *vs.* the Li^0/Li^+ couple. The discharge capacity of $LiCu_x^{II}Cu_y^{III}Mn_{[2-(x+y)]}^{III,IV}O_4$ was 71 mAh g^{-1} (97% of theoretical). Investigations have shown that the composition LMN possesses specific electrochemical characteristics such as a high capacity of 130–140 mAh g^{-1} associated to a high-voltage plateau at 4.7 V [55].

Figure 6. The energy *vs.* density of states showing the relative Fermi level of the $Ni^{4+/3+}$ and $Co^{4+/3+}$ redox couples for $Li_xNi_yMn_yCo_{1-2y}O_2$ during the charge, for three states of charge determined by the Li concentration x; (**a**) $x = 1$; (**b**) $x = 0.5$; (**c**) $x = 0$.

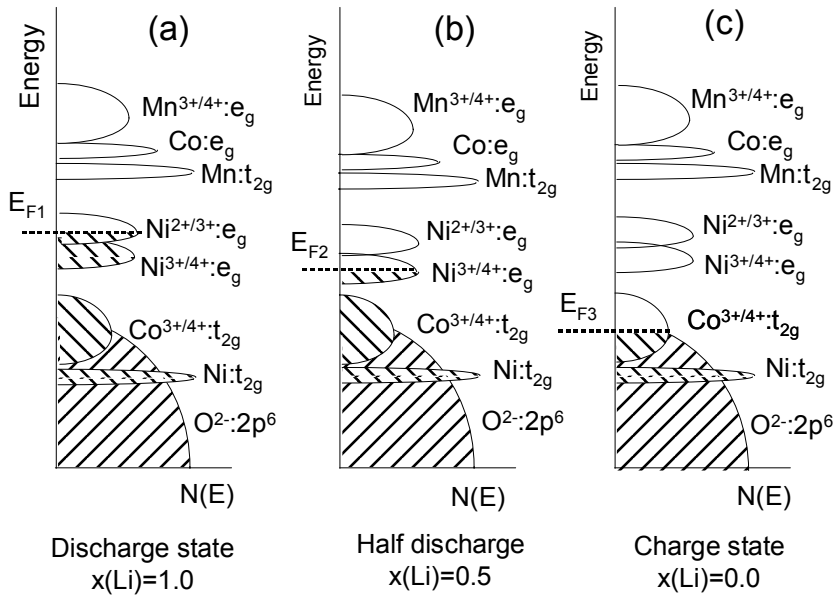

The electrochemical features show that the characteristic 4.1 V $Mn^{3+/4+}$ redox couple is always observed in the pristine or metal-doped LMN electrodes as a result of oxygen loss at high-temperature synthesis. However, no obvious 4.1 V step is detected in $LiMn_{1.45}Ni_{0.45}Cr_{0.1}O_4$ spinel, confirming that most of the residual Mn^{3+} ions have been re-oxidized to Mn^{4+} after re-annealing at 600 °C in agreement with the analysis of magnetic properties [26]. This is also consistent with the Rietveld refinement results. In order to understand the difference in the electrochemical properties of these electrode materials, Figure 7 compares the incremental capacity curves, dQ/dV *vs.* V graphs. Removal of Li from the tetrahedral sites of the spinel LMN framework initially probes the oxidation reaction of $Ni^{2+/3+}$ just below 4.7 V (typically ~4.69 V) for the disordered $Fd3m$ and above 4.7 V (typically ~4.72 V) for the ordered $P4_332$ spinels [56]. Ordering of the Ni and Mn raises by ~0.02 eV the $V(x)$ profile of LMN. From Figure 7, two anodic peaks at 4.663 and 4.731 V plus two cathodic peaks at

4.638 and 4.704 V are observed for the Cr-doped LMN, which is in agreement with two voltage plateaus for disordered LMN. Kim *et al.* suggested that as the crystallographic structure changed from *Fd*3*m* to $P4_332$, the voltage gaps between the two plateaus became narrower at around 4.75 V and resulted in a flatter voltage profile [57].

4.5. Lithium Iron Phosphate ($LiFePO_4$)

With theoretical specific capacity 170 mAh g^{-1} at moderate current densities, the phospho-olivine $LiFePO_4$ (LFP) is considered as potential positive electrode material for use in lithium rechargeable cells; it is inexpensive and not toxic, two determinant advantages with respect to cobalt-oxide-based materials for large-scaled applications such as hybrid electric vehicles (HEV). Nevertheless, the low electronic conductivity ($\sigma_e < 10^{-9}$ S cm^{-1}) and the low diffusion coefficient of Li^+ ion ($\widetilde{D} \approx 10^{-14}$ cm^2 s^{-1}) of LFP may result in losses in capacity during high-rate discharge. However, the reduction of the LFP particles to the nanosize provides short Li^+-ion diffusion paths within the positive electrode. In addition, the synthesis of carbon-coated LFP remarkably enhances the electrical conduction between particles ensuring high rate capability and preventing particles agglomeration [58–60].

Figure 7. Differential capacity curves, d*Q*/d*V* *vs.* *V*, of the (**a**) LMN and (**b**) Cr-doped LMN. The values at the peaks are given in volt [28].

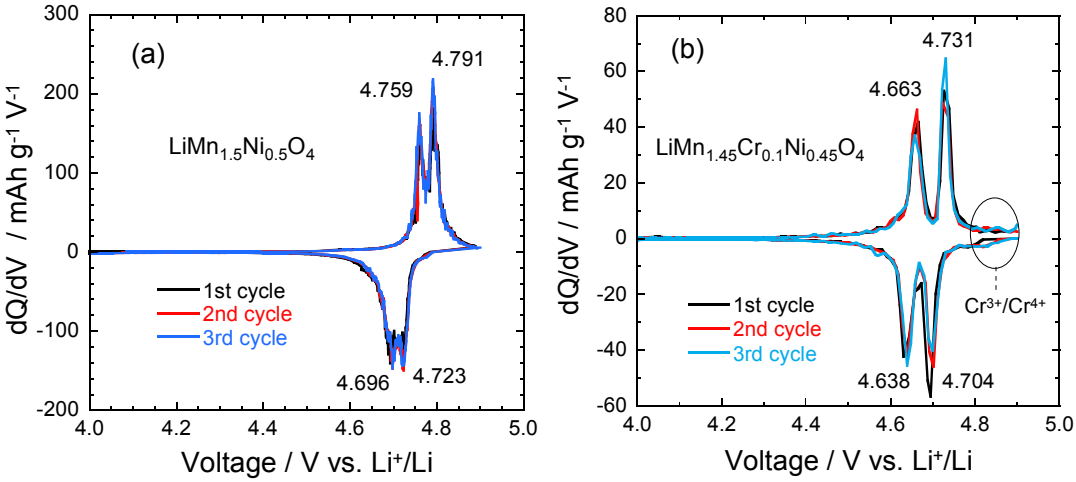

Electrochemical extraction of Li from $LiFePO_4$ gives (Fe^{2+}/Fe^{3+}) redox potential at ca. 3.45 V *vs.* Li^0/Li^+. A small but first-order displacive structural change of the framework gives a two-phase separation over most of the solid-solution range $0 < x < 1$ for Li_xFePO_4 and therefore a flat *V*-*x* curve. A reversible capacity ≈160 mAh g^{-1} is delivered by the nano-structured cathode particles coated with carbon. This result is attributed to the high quality of the "optimized" $LiFePO_4$, impurity-free materials used as positive electrodes. Figure 8a presents the voltage profiles of $LiFePO_4$//Li cells as a function of the preparation of the electrode material. These graphs show that without carbon coating, the specific capacity is lower than 100 mAh g^{-1}, while a 3-nm thick carbon film deposited onto 500-nm sized LFP particle enhances the discharge capacity to 141 mAh g^{-1} at C/12 rate [61,62].

The electrochemical performance of optimized LFP and LTO electrode materials has been tested separately in half cell with respect to Li metal anode, using the same usual electrolyte 1 mol L^{-1} $LiPF_6$

in ethlene carbonate (EC) and diethylene carbonate (DEC) [62,63]. The voltage *vs.* capacity curves recorded under such conditions at 25 °C are reported in Figure 8b at low C-rate C/24 to approach thermodynamic equilibrium together with the potential-capacity curve of the LTO//LFP lithium-ion battery. The voltage window is 2–4 V for $LiFePO_4$, 1.2–2.5 V for $Li_4Ti_5O_{12}$. Note in this figure (and the following ones), we have kept the conventional rule, *i.e.*, the capacity is in mAh per gram of the active element of the cathode. That is the reason why the maximum capacity for the LFP//Li and LFP//LTO cells are the same. For LFP//Li, the first coulombic efficiency is 100% and the reversible capacity is 148 mAh g^{-1}. For LTO, the first coulombic efficiency is 98% and the reversible capacity is 157 mAh g^{-1}. The well-known plateaus at 3.4 and 1.55 V are characteristics of the topotactic insertion/deinsertion of lithium in the two-phase systems $LiFePO_4$-$FePO_4$ and $Li_4Ti_5O_{12}$-$Li_7Ti_5O_{12}$, respectively [64].

Figure 8. (**a**) Electrochemical performance of the $LiFePO_4$//Li coin cell operating at room temperature before and after carbon coating. Charge-discharge cycling was conducted at the C/12 rate. (**b**) Voltage-capacity cycle for $LiFePO_4$//Li, $Li_4Ti_5O_{12}$//Li and Li-ion cell $LiFePO_4$//$Li_4Ti_5O_{12}$ at C/24 rate [62]. The capacity is in mAh per gram of the positive electrode element ($LiFePO_4$, $Li_4Ti_5O_{12}$ and $LiFePO_4$, respectively). The larger hysteresis in the $LiFePO_4$//$Li_4Ti_5O_{12}$ cell comes from the fact that the cell in that case was a button cell instead of the more elaborate 18650-cell, but the plateau at 1.9 V is well observed. All the cells used 1 mol L^{-1} $LiPF_6$ in EC:DEC (1:1) as electrolyte.

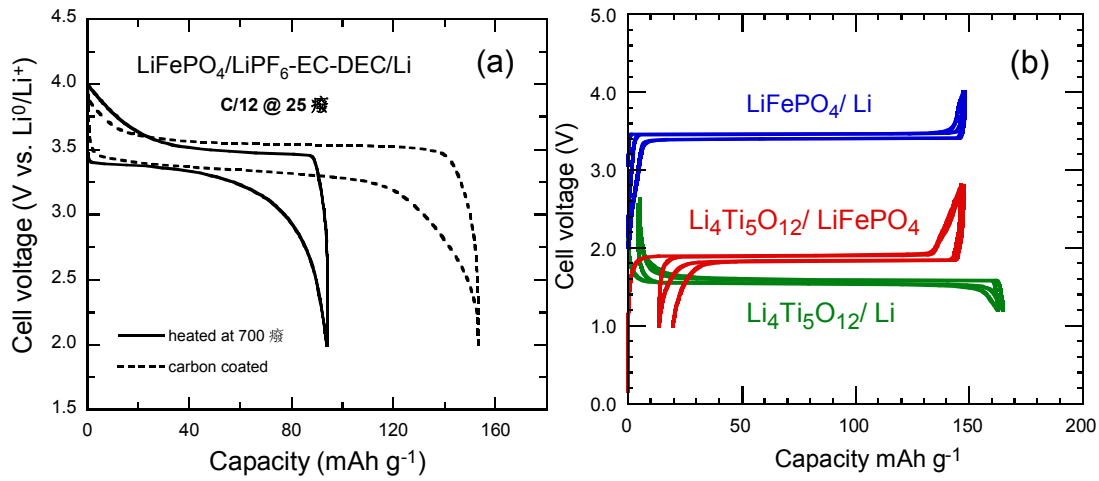

5. Safety Issues

5.1. Loss of Oxygen in Li_xCoO_2

The Li_xCoO_2 cathodes are known to cycle well for $x > 0.5$ and, therefore, no oxygen loss may occur in electrochemical cells. The observation of the beginning of oxygen loss at a slightly higher Li content $x \approx 0.45$ could be due to a rapid and deeper extraction of lithium on the surface although the average lithium content is >0.5, which may result in overall oxygen content slightly less than 2 for $0.5 \leq x \leq 0.45$. The band diagrams given in Figure 9 show the differences in the chemical instability with respect to oxygen loss due to the overlapping of the $Co^{4+/3+}$:t_{2g} band with the O:2*p* orbitals.

Chemical analysis of electrochemically charged $Li_{1-x}CoO_2$ samples indicates that the oxygen loss occurs below lithium content $x = 0.5$ [65]. The results suggest that the cobalt oxide system is intrinsically prone to lose oxygen for $x < 0.5$ in the Li-ion cells. The loss of oxygen from the lattice in the $Li_{1-x}CoO_2$ system may be one of the reasons for the limited capacity (140 mAh g^{-1}) leading to capacity fade. On the other hand, the absence of oxygen loss for $0.7 \leq x \leq 0$ in the $Li_xNi_{0.85}Co_{0.15}O_2$ system as well as the appearance of the second phase at a much lower lithium content $x < 0.77$ permit the realization of a higher capacity, *ca.* 180 mAh g^{-1}.

5.2. Comparative Safety Issues

Thermal stability for lithium-insertion compounds use as positive electrodes in Li-ion batteries has been studied for C-$LiFePO_4$, $LiNi_{0.8}Co_{0.15}Al_{0.05}O_2$, $LiNi_{0.33}Co_{0.33}Mn_{0.33}O_2$ and $LiCoO_2$ [66]. Figure 10 shows differential scanning calorimetry (DSC) spectra of the overcharged spinel ($LiMn_2O_4$), layered ($LiNi_{0.8}Co_{0.15}Al_{0.05}O_2$) cathode and carbon-coated $LiFePO_4$, all electrodes with traces of 1.2 mol L^{-1} $LiPF_6$ in ethylene carbonate:ethyl-methyl carbonate (3:7), measured at a scan rate of 10 °C min^{-1} from 50–400 °C. We can observe that both spinel and olivine cathodes have delayed onset temperature by at least 70 °C with respect to the layered cathode. The layered cathode was found to be thermally unsafe, as this cathode undergoes its exothermic reaction with very large enthalpy (−941 J g^{-1}) and the reaction is completed at much earlier temperature, lower than the onset temperature of spinel and olivine. Spinel cathode showed roughly half the exothermic reaction enthalpy (−439 J g^{-1}), whereas carbon-coated olivine showed even lesser exothermic reaction enthalpy (−250 J g^{-1}). The DSC results for layered, spinel and olivine positive electrodes are summarized in Table 2.

Figure 9. Change of the qualitative energy diagrams of Li_xCoO_2 as a function of the lithium content. From left to right: $x = 1$, $x = 0.5$, $x = 0$.

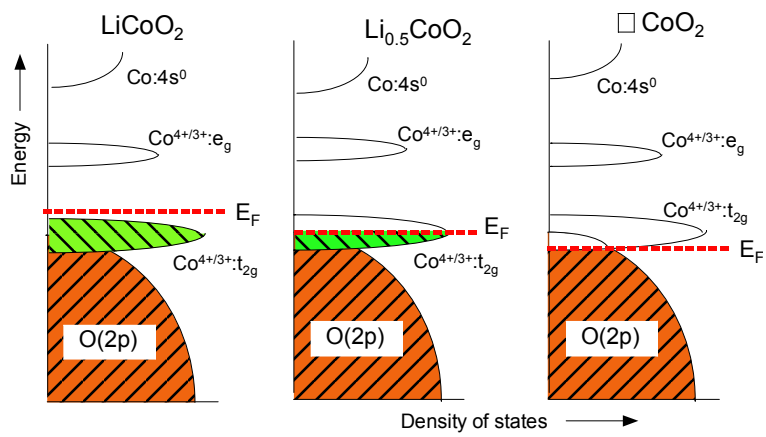

Based on their previous experimental results, Bang *et al.* [67] proposed that a possible mechanism leading to the thermal runaway of the layered cathode consists of the following four steps as follows: Step (1): The first step involves a partial structural deformation of $Li_xNi_{0.8}Co_{0.15}Al_{0.05}O_2$ into disorder oxide (spinel-like structure) and liberation of small amount of oxygen from it as a result of this structural deformation. Step (2): This step entails the reaction of the oxygen produced in Step (1) with the ethylene carbonate due to its lower flash point of 150 °C

$$C_3H_4O_3 + 2.5O_2 \rightarrow 3CO_2 + 2H_2O \quad (4)$$

The continuous reaction of the oxygen with EC and possibly EMC releases combustion heat in the system and raises the temperature, Step (3): The heat released in the above reaction further accelerates the structural deformation, which finally leads to complete structural collapse of the oxide

$$Li_{0.36}Ni_{0.8}Co_{0.15}Al_{0.05}O_2 \rightarrow 0.18Li_2O + 0.8\ NiO + 0.05Co_3O_4 + 0.025Al_2O_3 + 0.372O_2 \quad (5)$$

Finally, Step (4): The large amount of oxygen and heat produced in the above reaction helps the combustion of the remaining electrolyte (EC, EMC, and $LiPF_6$) to produce thermal runaway

$$C_3H_4O_3 + 2.5O_2 \rightarrow 3CO_2 + 2H_2O \quad (6)$$

$$C_3H_8O_3 + 2.5O_2 \rightarrow 3CO_2 + 2H_2O \quad (7)$$

However, in $LiFePO_4$, the phase transformation to $FePO_4$ is considered to occur in Step (1) rather than structure disordering observed in a layered cathode. Step (2) is observed to the same extent found in layered cathode, whereas Step (3) is mostly prevented as the heat released from combustion of the solvents with O_2 is used to maintain the $FePO_4$ phase, hence the structural stability of the $LiFePO_4/FePO_4$ cathode. Again, the strong P-O covalent bonds in $(PO_4)^{3-}$ polyanion found in $LiFePO_4$ significantly reduce the rate of O_2 release, thereby reducing the combustion step itself and causing no further damage to the cathode structure.

Figure 10. DSC spectra of over charged layered, spinel and olivine cathodes with traces of 1.2 mol L^{-1} $LiPF_6$ in EC-EMC (3:7) electrolyte at 10 °C min^{-1} [66].

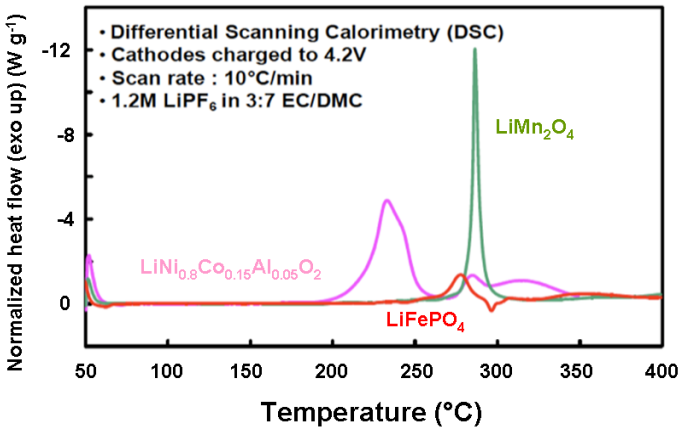

Table 2. Flow of enthalpy deduced from the DSC spectra of the fully delithiated and over charged carbon-coated $LiFePO_4$ and the fully lithiated carbon-coated graphite that of the overcharged cathode elements investigated are reported in the three last columns.

Cathode material	Onset *T* (°C)	Overall ΔH (J g^{-1})
$LiNi_{0.8}Co_{0.15}Al_{0.05}O_2$	170	−941
$LiMn_2O_4$	264	−439
$LiFePO_4$	245	−250

Isothermal micro-calorimetry (IMC) measurements on $LiFePO_4$ have shown that the cell temperature is raised to not more than 34 °C during charge and discharge at 0.5C rate, and DSC measurements showed that $LiFePO_4$ is less reactive with electrolyte at high temperatures than spinel and layered cathodes. Moreover, fully lithiated graphite was observed to show more exothermic heat than $LiFePO_4$ cathode itself, resulting from SEI layer decomposition. So, a fully charged cylindrical 18,650 cell using $LiFePO_4$/graphite was tested in Accelerating Rate Calorimeter (ARC) to realize the overall combination of exothermic reaction heats of $LiFePO_4$, graphite and electrolyte [66]. The simultaneous cell temperature and heater temperature and *in-situ* cell open-circuit potential recorded during the ARC test of the cell is reported in Figure 11. It shows that the cell was heated uniformly as the thermocouples placed on top, side and base of the heater indicated the same temperature during the course of the experiment, and the cell temperature also closely followed the heater temperature until any self-heat was released from the cell. Open-circuit potential remained constant around 3.3 V during this period. At a temperature of about 80 °C after 160 min from the start of the experiment, the cell started to show self-heat at a rate greater than 0.02 °C min^{-1}. Once the self-heat is released from the cell and is sustained for more than 30 min, the heater begins to follow the cell temperature to the same rate of self-heat. Open-circuit potential also began to gradually drop due to the resistive heating of the cell. After 1455 min of testing, the cell temperature began to rise sharply at a temperature of 150 °C and open-circuit potential began to drop rapidly. This behavior of the cell was attributed to an internal short-circuit of the cell owing to the melting of the separator. At 1756 min of testing, the cell completely decomposed and the cell temperature completely shot off from that of the heater temperature by more than 80 °C; the cell voltage abruptly fell close to zero a few minutes later.

Figure 11. Cell temperature measured at side, top and base of the heater (the curves are superposed) and *in-situ* open-circuit potential chronological record of $LiFePO_4$/C 18,650 cell subjected to an ARC test [66].

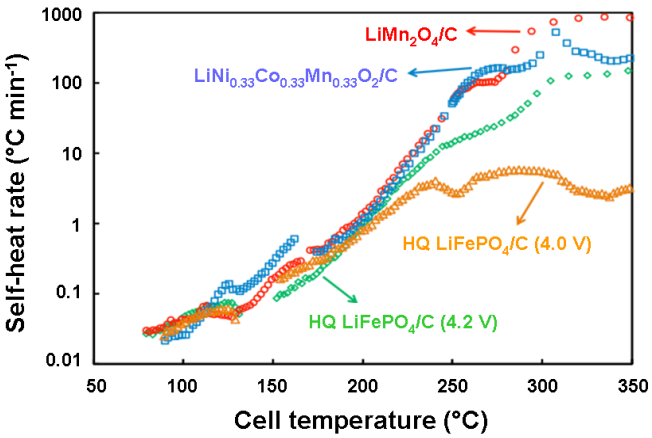

6. Concluding Remarks

The development of various lithium insertion compounds over the years has made lithium-ion batteries a commercial reality as listed in Table 3. The transition-metal oxides crystallizing in rock salt-based layer, spinel and olivine structures such as Li_xMO_2 (M = Co, Ni, $Ni_{1-y}Co_yO_2$), LiM'_2O_4

(M' = Mn, $Ni_{1/4}Mn_{3/4}$) and $LiFePO_4$. These hosts having highly oxidized $M^{4+/3+}$ and $M^{3+/2+}$ redox couples emerge as the leading candidates for positive electrodes.

The principal challenges facing the development of suitable hosts with compatible anodes for the next generation Li-ion cells for either portable electronic or electric vehicles request several considerations: chemical and structural stabilities, capacity electrode, voltage, rate capability, service life and thermal safety. Long service life requires elimination of unwanted chemical reactions between electrode materials and the electrolyte. The good capacity retention over many charge-discharge cycles restricts the volume change *vs.* state of charge of the active electrode material. Safety is related to the flammability of the electrolyte, the rate of charge and/or discharge and the structural stability, *i.e.*, absence of oxygen produced by the structural collapse of the cathode. Both the $LiFePO_4$ cathode and the $Li_4Ti_5O_{12}$ anode have demonstrated safe and rapid charge and discharge over many cycles. Their chemical potential is located within the electrolyte window ($\mu_C - \mu_A < E_g$), which removes the requirement of a passivating SEI layer (Figure 12).

Table 3. Configuration of the three types of Li-ion cells related to their application. Positive electrodes are either layered (L), spinel (S) or olivine (O) frameworks.

Application	Positive electrode	Negative electrode	Remarks
High energy	$LiCoO_2$ (L) $LiNi_yCo_zM_{1-y-z}O_2$ (L) $LiMn_2O_4$ (S)	Graphite, Si, SnO_x, CoO_x, FeO_x, CuO_x, NiO_x, *etc.*	M = Mn, Al, Cr named "LMO"
High power	$LiMn_{2-y}Al_yO_{4+\delta}$ (S) $LiNi_yMn_yCo_{2-y}O_2$ (L) $LiFePO_4$ (O)	hard carbon, graphite $Li_4Ti_5O_{12}$ (S)	named "NMC" "LFP//LTO" cell
Long cycle life	$LiMn_{2-y}Al_yO_{4+\delta}$ (S) $LiFePO_4$ (O) $LiFe_{1-y}Mn_yPO_4$ (O)	Graphite $Li_4Ti_5O_{12}$ (S) $Li_4Ti_5O_{12}$ (S)	named "LFP"

Figure 12. Schematic comparison between the LCO//graphite and the LFP//LTO cells. (**a**) Ideal battery where potential $E_A - E_C < E_g$, the voltage of the battery is equal to the energy difference $V = E_C - E_A$; (**b**) The conventional graphite//$LiCoO_2$ Li-ion battery where $E_A - E_C > E_g$; this cell works through the formation of the SEI; (**c**) The HQ-type LTO//LFP Li-ion battery where $E_A - E_C < E_g$; this cell operates without the formation of the SEI.

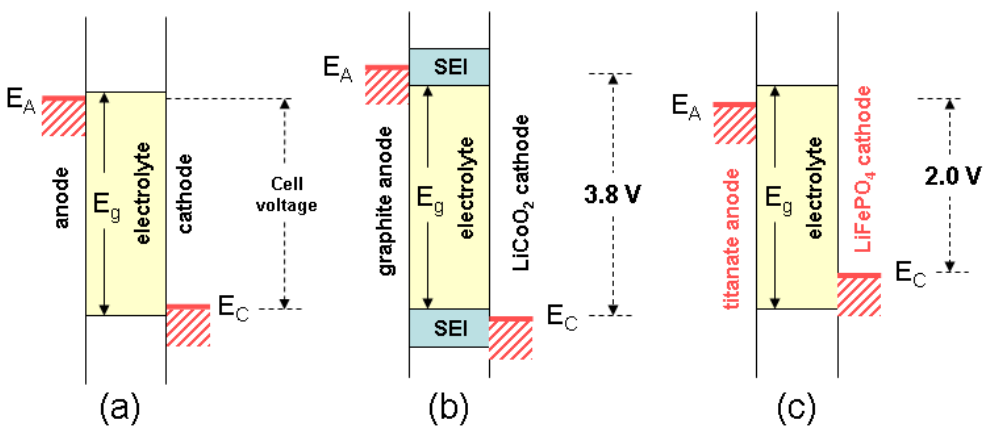

Reducing the particle size or designing the architecture of the electrode material to the nanoscale level is one of the options abovementioned and can lead to improvement in the electrochemical performance. The reduced diffusion path length for Li^+ ions and electrons increase particularly the rate of charge or discharge as the characteristic time, τ, is given by $\tau = L^2/4\pi\widetilde{D}$, where L is the particle size and $\widetilde{D}$ the diffusion coefficient of Li^+ ion in the host lattice. As an example, for 2-µm $LiFePO_4$ particles τ = 83 h, while decreasing the particle to 40 nm reduces τ to 13 s. The volume changes caused by Li^+ insertion/extraction are better accommodated by nanosized particles due to faster strain relaxation. However, a few disadvantages are: (i) the need of surface coating for either minimizing the reaction at the electrode-electrolyte interface for LCO and LMO or enhanced the electrical contact between particles for LFP; (ii) the increase of the specific surface area of nanoparticles could enhance the rate reaction at the interfaces, especially for LCO material and (iii) the lower density of the electrode material, which reduces the volumetric capacity.

From the safety view point, a comparison of the schematic representation (Figure 12) between the graphite//LCO and the LTO//LFP cells could be considered, as a safe battery delivers a potential equal to $E_A - E_C < E_g$. However, conventional battery works through formation of a passivation layer on the surface of electrodes, the so-called "SEI" (Figure 12b). This layer grows over time, increasing the internal resistance of the battery. Abuse of operation produces a considerable local heating (>200 °C), resulting in the decomposition of the electrolyte from the cathode but also by producing oxygen, which ignites the electrolyte. Several accidents have occurred: laptop in Chicago, EVs in Shanghai, fire in *Dreamliner* aircrafts, *etc.* Only the Li-ion battery fourth generation iron phosphate//titanate ($LiFePO_4/Li_4Ti_5O_{12}$) is highly secure. The first reason is the position of the energy levels located inside the electrolytic window ensuring the absence of formation of SEI (Figure 12c). The second reason is that the oxygen in $LiFePO_4$ and the phosphorous atoms are strongly linked by covalent bonding to form the PO_4^{3-} ion, which can be broken only at potential of 5.4 V, which insures the lack of production of the oxidant (O_2) up to this potential.

The performance of olivine $LiFePO_4$ has been improved and insertion/de-insertion mechanism has been understood. However, there are still some problems to be solved, especially for its volumetric energy density and low temperature performance. The Hydro-Québec group showed the incomparable safety of this Li-ion battery which is the only one that passes the crushing and perforation tests without the need of any battery monitoring system. Studies in 2011 showed that iron-phosphate//titanate batteries can be cycled 30,000 times without capacity loss. As the promising cathode materials of the next generation of large-scale lithium-ion battery for EVs or HEVs, $LiFePO_4$ is almost ready.

Many efforts are currently made on Li- and Mn-rich compounds, in particular $Li[Li_xMn_{1-x-2y}Co_yNi_y]O_2$ and $LiMn_{1.5}Ni_{0.5}O_4$. The high voltage (4.7 V) is still inside the electrolyte window, and the discharge capacity is also high (250 mAh g^{-1}). Owing to these two properties, these materials have an energy density much higher than the other reported cathode oxides and are then the most promising cathode candidates for high-energy density Li-ion batteries for EV applications. The drawback of the high operating voltage, however, is the relative structural instability of the material against a loss of oxygen. The kinetics of this loss of oxygen increases with temperature, so that the $LiMn_{1.5}Ni_{0.5}O_4$-based cells deteriorate too fast at ~50 °C to be used for EV applications. Many efforts are currently made to remedy this situation by surface modifications. In particular, coating the particles with a protective

layer that prevents the oxygen from outgoing has led to major improvements, but the problem has not been entirely resolved, mainly because the coating with such compounds like $LiFePO_4$ is only partial. Efforts must be directed toward developing a coating to make it complete and uniform, and to make the development of the 5-V batteries a reality.

Conflicts of Interest

The authors declare no conflict of interest.

References

1. Nagaura, T.; Tozawa, K. Lithium ion rechargeable battery. *Prog. Batter. Sol. Cells* **1990**, *9*, 209–211.
2. Mizushima, K.; Jones, P.C.; Wiseman, P.J.; Goodenough, J.B. Li_xCoO_2 ($0 < x < 1$): A new cathode material for batteries of high energy density. *Mater. Res. Bull.* **1980**, *15*, 783–789.
3. Thackeray, M.M.; David, W.I.F.; Bruce, P.G.; Goodenough, J.B. Lithium insertion into manganese spinels. *Mater. Res. Bull.* **1983**, *18*, 461–472.
4. Thackeray, M.M.; Johnson, P.J.; de Picciotto, L.A.; Bruce, P.G.; Goodenough, J.B. Lithium extraction from $LiMn_2O_4$. *Mater. Res. Bull.* **1984**, *19*, 179–187.
5. Padhi, A.K.; Nanjundaswamy, K.S.; Goodenough, J.B. Phospho-olivines as positive-electrode materials for rechargeable lithium batteries. *J. Electrochem. Soc.* **1997**, *144*, 1188–1194.
6. Peres, J.P.; Weill, F.; Delmas, C. Lithium-vacancy ordering in the monoclinic Li_xNiO_2 ($0.50 < x < 0.75$) solid solution. *Solid State Ion.* **1999**, *116*, 19–27.
7. Ohzuku, T.; Makimura, Y. Layered lithium insertion material of $LiCo_{1/3}Ni_{1/3}Mn_{1/3}O_2$ for lithium-ion batteries. *Chem. Lett.* **2001**, *30*, 642–643.
8. Tarascon, J.M.; McKinnon, W.R.; Coowar, F.; Bowmer, T.N.; Amatucci, G.; Guyomard, D. Synthesis conditions and oxygen stoichiometry effects on Li insertion into the spinel $LiMn_2O_4$. *J. Electrochem. Soc.* **1994**, *141*, 1421–1431.
9. Zaghib, K.; Mauger, A.; Groult, H.; Goodenough, J.B.; Julien, C.M. Advanced electrodes for high power Li-ion batteries. *Materials* **2013**, *6*, 1028–1049.
10. Goodenough, J.B. Design considerations. *Solid State Ion.* **1994**, *69*, 184–198.
11. Goodenough, J.B.; Kim, Y. Challenges for rechargeable Li batteries. *Chem. Mater.* **2010**, *22*, 587–603.
12. Liu, D.; Han, J.; Dontigny, M.; Charest, P.; Guerfi, A.; Zaghib, K.; Goodenough, J.B. Redox behaviors of Ni and Cr with different counter cations in spinel cathodes for Li-ion batteries. *J. Electrochem. Soc.* **2010**, *157*, A770–A775.
13. Goodenough, J.B. Oxides cathodes. In *Advances in Lithium-Ion Batteries*; Kluwer Academic/Plenum: New York, NY, USA, 2002; pp. 135–154.
14. Manthiram, A. Chemical and Structural Stabilities of Layered Oxide Cathodes. In *New Trends in Intercalation Compounds for Energy Storage, NATO Science Series*; Kluwer Academic Publishers: Dordrecht, The Netherlands, 2002; pp. 177–192.
15. Thackeray, M.M. Structural considerations of layered and spinel lithiated oxides for lithium io batteries. *J. Electrochem. Soc.* **1995**, *142*, 2558–2563.

16. Julien, C. Local cationic environment in lithium nickel–cobalt oxides used as cathode materials for lithium batteries. *Solid State Ion.* **2000**, *136–137*, 887–896.
17. Arroyo y de Dompablo, M.E.; Marianetti, C.; van der Ven, A.; Ceder, G. Jahn-Teller mediated ordering in layered Li_xCoO_2 compounds. *Phys. Rev. B* **2001**, *63*, 144104, doi:10.1103/PhysRevB.63.144107.
18. Li, X.; Liu, J.; Meng, X.; Tang, Y.; Banis, M.N.; Yang, J.; Hu, Y.; Li, R.; Cai, M.; Sun, X. Significant impact on cathode performance of lithium-ion batteries by precisely controlled metal oxide nanocoatings via atomic layer deposition. *J. Power Sources* **2013**, *247*, 57–69.
19. Li, X.; Liu, J.; Banis, M.N.; Lushington, A.; Li, R.; Caib, M.; Sun, X. Atomic layer deposition of solid-state electrolyte coated cathode materials with superior high voltage cycling behavior for lithium ion battery application. *Energy Environ. Sci.* **2014**, *7*, 768–778.
20. Ohzuku, T.; Ueda, A.; Nagayama, M.; Iwakashi, Y.; Komori, H. Comparative study of $LiCoO_2$, $LiNi_{1/2}Co_{1/2}O_2$ and $LiNiO_2$ for 4 volt secondary lithium cells. *Electrochim. Acta* **1993**, *38*, 1159–1167.
21. Delmas, C.; Saadoune, I. Electrochemical and physical properties of $Li_xNi_{1-y}Co_yO_2$ phases. *Solid State Ion.* **1992**, *53–56*, 370–375.
22. Rougier, A.; Saadoune, I.; Gravereau, P.; Willmann, P.; Delmas, C. Effect of cobalt substitution on cationic distribution in Li electrode materials. *Solid State Ion.* **1996**, *90*, 83–90.
23. Julien, C.; El-Farh, L.; Rangan, S.; Massot, S. Synthesis of $LiNi_{1-y}Co_yO_2$ cathode materials prepared by a citric acid-assisted sol-gel method for lithium batteries. *J. Sol-Gel Sci. Technol.* **1999**, *15*, 63–72.
24. Li, W.; Curie, J. Morphology effects on the electrochemical performance of $LiNi_{1-x}Co_xO_2$. *J. Electrochem. Soc.* **1997**, *144*, 2773–2779.
25. Ohzuku, T.; Kitagawa, M.; Hirai, T. Electrochemistry of manganese dioxide in lithium nonaqueous cell: III. X-ray diffractional study on the reduction of spinel-related manganese dioxide. *J. Electrochem. Soc.* **1990**, *137*, 769–775.
26. Yonemura, M.; Kamiyama, T.; Kawamoto, Y.; Kanno, R. Phase transitions and low-temperature structure of lithium manganese oxide spinel. *Mater. Trans.* **2004**, *45*, 2048–2055.
27. Zhong, Q.M.; Bonakdarpour, A.; Zhang, M.J.; Gao, Y.; Dahn, J.R. Synthesis and electrochemistry of $LiNi_xMn_{2-x}O_4$. *J. Electrochem. Soc.* **1997**, *144*, 205–213.
28. Liu, D.; Hamel-Paquet, J.; Trottier, J.; Barray, F.; Gariépy, V.; Hovington, P.; Guerfi, A.; Mauger, A.; Julien, C.M.; Goodenough, J.B.; *et al*. Synthesis of pure phase disordered $LiMn_{1.45}Cr_{0.1}Ni_{0.45}O_4$ by a post-annealing method. *J. Power Sources* **2012**, *217*, 400–406.
29. Geller, S.; Durand, J.L. Refinement of the structure of $LiMnPO_4$. *Acta Crystallogr.* **1960**, *13*, 325–331.
30. Santorro, R.P.; Newnham, R.E. Antiferromagnetism in $LiFePO_4$. *Acta Crystallogr.* **1967**, *22*, 344–347.
31. Moring, J.; Kostiner, E. The crystal structure of $NaMnPO_4$. *J. Solid State Chem.* **1986**, *61*, 379–383.

32. Zaghib, K.; Mauger, A.; Goodenough, J.B.; Gendron, F.; Julien, C.M. Design and properties of $LiFePO_4$ positive electrode materials for Li-ion batteries. In *Advanced Materials and Methods for Lithium-ion Batteries*; Zhang, S.S., Ed.; Transworld Research Network: Trivandrum, India, 2007; pp. 115–149.
33. Laubach, S.; Laubach, S.; Schmidt, P.C.; Ensling, D.; Schmid, S.; Jaegermann, W.; Thisen, A.; Nikolowski, K.; Ehrenberg, H. Changes in the crystal and electronic structure of $LiCoO_2$ and $LiNiO_2$ upon Li intercalation and de-intercalation. *Phys. Chem. Chem. Phys.* **2009**, *11*, 3278–3289.
34. Reimers, J.N.; Dahn, J.R. Electrochemical and *in situ* X-ray diffraction studies of lithium intercalation in Li_xCoO_2. *J. Electrochem. Soc.* **1992**, *139*, 2091–2097.
35. Van der Ven, A.; Aydinol, M.K.; Ceder, G.; Kresse, G.; Hafner, J. First-principles investigation of phase stability in Li_xCoO_2. *Phys. Rev. B* **1998**, *58*, 2975–2987.
36. Chen, Z.; Dahn, J.R. Methods to obtain excellent capacity retention in $LiCoO_2$ cycled to 4.5 V. *Electrochim. Acta* **2004**, *49*, 1079–1090.
37. Amatucci, G.G.; Schmutz, C.N.; Blyr, A.; Sigala, C.; Gozdz, A.S.; Larcher, D.; Tarascon, J.M. Materials effects on the elevated and room temperature performance of $C/LiMn_2O_4$ Li-ion batteries. *J. Power Sources* **1997**, *69*, 11–25.
38. Thackeray, M.M. Manganese oxides for lithium batteries. *Prog. Solid State Chem.* **1997**, *25*, 1–71.
39. Xia, Y.; Zhou, Y.; Yoshio, M. Capacity fading on cycling of 4 V $Li/LiMn_2O_4$ cells. *J. Electrochem. Soc.* **1997**, *144*, 2593–2600.
40. Dai, Y.; Cai, L.; White, R.E. Capacity fade model for spinel $LiMn_2O_4$ electrode. *J. Electrochem. Soc.* **2013**, *160*, A182–A190.
41. Jang, D.H.; Oh, S.M. Electrolyte effects on spinel dissolution and cathodic capacity losses in 4-V $Li/Li_xMn_2O_4$ rechargeable cells. *J. Electrochem. Soc.* **1997**, *144*, 3342–3348.
42. Gnanaraj, J.S.; Pol, V.G.; Gedanken, A.; Aurbach, D. Improving the high-temperature performance of $LiMn_2O_4$ spinel electrodes by coating the active mass with MgO via a sonochemical method. *Electrochem. Commun.* **2003**, *5*, 940–945.
43. Walz, K.A.; Johnson, C.S.; Genthe, J.; Stoiber, L.C.; Zeltner, W.A.; Anderson, M.A.; Thackeray, M.M. Elevated temperature cycling stability and electrochemical impedance of $LiMn_2O_4$ cathodes with nanoporous ZrO_2 and TiO_2 coatings. *J. Power Sources* **2010**, *195*, 4943–4951.
44. Kannan, A.M.; Manthiram, A. Surface chemically modified $LiMn_2O_4$ cathodes for lithium-ion batteries. *Electrochem. Solid-State Lett.* **2002**, *5*, A167–A169.
45. Amatucci, G.G.; Blyr, A.; Sigala, C.; Alfonse, P.; Tarascon, J.M. Surface treatments of $Li_{1+x}Mn_{2-x}O_4$ spinels for improved elevated temperature performance. *Solid State Ion.* **1997**, *104*, 13–25.
46. Lee, D.J.; Lee, K.S.; Myung, S.T.; Yashiro, H.; Sun, Y.K. Improvement of electrochemical properties of $Li_{1.1}Al_{0.05}Mn_{1.85}O_4$ achieved by an AlF_3 coating. *J. Power Sources* **2011**, *196*, 1353–1357.
47. Gummow, R.J.; de Kock, A.; Thackeray, M.M. Improved capacity retention in rechargeable 4V lithium/lithium manganese oxide (spinel) cells. *Solid State Ion.* **1994**, *69*, 59–67.
48. Park, O.K.; Cho, Y.; Yoo, H.C.; Song, H.K.; Cho, J. Who will drive electric vehicles, olivine or spinel? *Energy Environ. Sci.* **2011**, *4*, 1621–1633.

49. Thackeray, M.M.; Shao-Horn, Y.; Kahaian, A.J.; Kepler, K.D.; Skinner, E.; Vaughey, J.T.; Hackney, S.A. Structural fatigue in spinel electrodes in high voltage (4 V) Li/$Li_xMn_2O_4$ cells. *Electrochem. Solid-State Lett.* **1998**, *1*, 7–9.
50. Lee, Y.J.; Wang, F.; Mukerjee, S.; James McBreen, J.; Grey, C.P. ^{6}Li and ^{7}Li magic-angle spinning nuclear magnetic resonance and *in situ* X-ray diffraction studies of the charging and discharging of $Li_xMn_2O_4$ at 4 V. *J. Electrochem. Soc.* **2000**, *147*, 803–812.
51. Yabuuchi, N.; Ohzuku, T. Novel lithium insertion material of $LiCo_{1/3}Ni_{1/3}Mn_{1/3}O_2$ for advanced lithium-ion batteries. *J. Power Sources* **2003**, *119–121*, 171–174.
52. Shaju, K.M.; Subba Rao, G.V.; Chowdari, B.V.R. Performance of layered $Li(Ni_{1/3}Co_{1/3}Mn_{1/3})O_2$ as cathode for Li-ion batteries. *Electrochim. Acta* **2002**, *48*, 145–151.
53. Zhang, X.-Y.; Jiang, W.-J.; Mauger, A.; Lu, Q.; Gendron, F.; Julien, C.M. Minimization of the cation mixing in $Li_{1+x}(NMC)_{1-x}O_2$ as cathode material. *J. Power Sources* **2010**, *195*, 1292–1301.
54. Ein-Eli, Y.; Howard, W.F., Jr. $LiCu_x^{II}Cu_y^{III}Mn_{[2-(x+y)]}^{III,IV}O_4$: 5 V cathode materials. *J. Electrochem. Soc.* **1997**, *144*, L205–L207.
55. Julien, C.M.; Mauger, A. Review of 5-V electrodes for Li-ion batteries: Status and trends. *Ionics* **2013**, *19*, 951–988.
56. Kunduraci, M.; Amatucci, G.G. Effect of oxygen non-stoichiometry and temperature on cation ordering in $LiMn_{2-x}Ni_xO_4$ ($0.50 \geq x \geq 0.36$) spinels. *J. Power Sources* **2007**, *165*, 359–367.
57. Kim, J.-H.; Yoon, C.S.; Myung, S.-T.; Prakash, J.; Sun, Y.-K. Phase transitions in $Li_{1-\delta}Ni_{0.5}Mn_{1.5}O_4$ during cycling at 5 V. *Electrochem. Solid-State Lett.* **2004**, *7*, A216–A220.
58. Wang, J.; Sun, X. Understanding and recent development of carbon coating on $LiFePO_4$ cathode materials for lithium-ion batteries. *Energy Environ. Sci.* **2012**, *5*, 5163–5185.
59. Wang, J.; Yang, J.; Tang, Y.; Li, R.; Liang, G.; Sham, T.K.; Sun, X. Surface aging at olivine $LiFePO_4$: A direct visual observation of iron dissolution and the protection role of nano-carbon coating. *J. Mater. Chem. A* **2013**, *1*, 1579–1586.
60. Wang, J.; Yang, J.; Zhang, Y.; Li, Y.; Tang, Y.; Banis, M.N.; Li, X.; Liang, G.; Li, R.; Sun, X. Interaction of carbon coating on $LiFePO_4$: A local visualization study of the influence of impurity phases. *Adv. Funct. Mater.* **2013**, *23*, 806–814.
61. Zaghib, K.; Guerfi, A.; Hovington, P.; Vijh, A.; Trudeau, M.; Mauger, A.; Goodenough, J.B.; Julien, C.M. Review and analysis of nanostructured olivine-based lithium rechargeable batteries: Status and trends. *J. Power Sources* **2013**, *232*, 357–369.
62. Zaghib, K.; Dontigny, M.; Guerfi, A.; Charest, P.; Rodrigues, I.; Mauger, A.; Julien, C.M. Safe and fast-charging Li-ion battery with long shelf life for power applications. *J. Power Sources* **2011**, *196*, 3949–3954.
63. Zaghib, K.; Dontigny, M.; Guerfi, A.; Trottier, J.; Hamel-Paquet, J.; Gariepy, V.; Galoutov, K.; Hovington, P.; Mauger, A.; Groult, H.; *et al.* An improved high-power battery with increased thermal operating range: C-$LiFePO_4$//C-$Li_4Ti_5O_{12}$. *J. Power Sources* **2012**, *216*, 192–200.
64. Julien, C.M.; Zaghib, K.; Mauger, A.; Groult, H. Enhanced electrochemical properties of $LiFePO_4$ as positive electrode of Li-ion batteries for HEV application. *Adv. Chem. Eng. Sci.* **2012**, *2*, 321–329.
65. Venkatraman, S.; Shin, Y.; Manthiram, A. Phase relationships and structural and chemical stabilities of charged $Li_{1-x}CoO_{2-\delta}$ and $Li_{1-x}Ni_{0.85}Co_{0.15}O_{2-\delta}$. *Electrochem. Solid State Lett.* **2003**, *6*, A9–A12.

66. Zaghib, K.; Dubé, J.; Dallaire, A.; Galoustov, K.; Guerfi, A.; Ramanathan, M.; Benmayza, A.; Prakash, J.; Mauger, A.; Julien, C.M. Enhanced thermal safety and high power performance of carbon-coated $LiFePO_4$ olivine cathode for Li-ion batteries. *J. Power Sources* **2012**, *219*, 36–44.
67. Bang, H.J.; Joachin, H.; Yang, H.; Amine, K.; Prakash, J. Contribution of the structural changes of $LiNi_{0.8}Co_{0.15}Al_{0.05}O_2$ cathodes on the exothermic reactions in Li-ion cells. *J. Electrochem. Soc.* **2006**, *153*, A731–A737.

© 2014 by the authors; licensee MDPI, Basel, Switzerland. This article is an open access article distributed under the terms and conditions of the Creative Commons Attribution license (http://creativecommons.org/licenses/by/3.0/).